The Astrophysical Journal, 639:781–787, 2006 March 10

DIRECT MEASUREMENTS OF GAS BULK FLOWS IN THE INTRACLUSTER MEDIUM OF THE CENTAURUS CLUSTER WITH THE *CHANDRA* SATELLITE

Renato A. Dupke and Joel N. Bregman
Department of Astronomy, University of Michigan, Ann Arbor, MI 48109-1090
Received 2004 November 24; accepted 2005 November 1

ABSTRACT

We present the analysis of the velocity structure of the intracluster gas near the core of Abell 3526 obtained with two off-center *Chandra* observations, specifically designed to eliminate errors due to spatial variations of the instrumental gain. We detected a significant velocity gradient along the northeast-southwest direction, roughly perpendicular to the direction of the incoming subgroup Cen 45, in agreement with previous *ASCA* SIS measurements. The presence of gas bulk velocities is observed both with and without the inclusion of the Fe K line complex in the spectral fittings. The configuration and magnitude of the velocity gradient is consistent with near transonic circulatory motion, either bulk or eddylike. The velocity difference obtained using the best calibrated central regions of ACIS-S3 is found to be $(2.4 \pm 1.0) \times 10^3$ km s^{-1} for rectangular regions $2.'4 \times 3'$ roughly diametrically opposed around the cluster's core. There are also indications of a high-velocity zone toward the southern region with similar magnitudes. The detection of velocity gradients is significant at >99.4% confidence, and simulations show that intrachip gain fluctuations >1800 km s^{-1} are required to explain the velocity gradient by chance. The measurements suggest that >1% of the total merger energy can still be bulk kinetic 0.4 Gyr after the merging event. This is the first direct confirmation of velocity gradients in the intracluster gas with independent instruments and indicates that strong departure from hydrostatic equilibrium is possible even for cool clusters that do not show obvious signs of merging.

Subject headings: cooling flows — galaxies: clusters: individual (Abell 3526) — intergalactic medium — X-rays: galaxies

1. INTRODUCTION

Clusters of galaxies form by the infall/merging of smaller scale systems. The merging of subclusters or groups of galaxies produces many intracluster gas signatures, such as temperature and density inhomogeneities and gas bulk motions, all of which are observable in X-rays. The comparison of temperature and surface brightness distributions to numerical simulations of mergers can tell us about the evolutionary stage of clusters (e.g., Evrard 1990; Katz & White 1993; Roettiger et al. 1993, 1996; Pearce et al. 1994; Navarro et al. 1995; Evrard et al. 1996). In particular, simulations predict that long-lasting gas bulk motions and turbulence will often appear as a consequence of cluster merging (e.g., Ricker 1998; Roettiger et al. 1998; Takizawa & Mineshige 1998; Burns et al. 2002; Takizawa 1999, 2000; Roettiger & Flores 2000; Ricker & Sarazin 2001; Pawl et al. 2005; Fujita et al. 2004). Since the intracluster medium (ICM) is enriched with heavy elements, gas velocities can be detected through the Doppler shift of spectral lines (Dupke & Bregman 2001a, 2001b, hereafter DB01a and DB01b, respectively), line broadening (Sunyaev et al. 2003; Pawl et al. 2005), and also through the kinetic Sunyaev-Zel'dovich effect using bolometers (Dupke & Bregman 2002; Sunyaev et al. 2003).

Previous X-ray studies of the physical state of the ICM have concentrated mostly on the analysis of temperatures, density, and metal abundance distributions. In order to zero in the precise evolutionary history of galaxy clusters and to determine the level of departure from hydrostatic equilibrium, it is very important to take into account gas velocities, a critical diagnostic that has largely been missing from cluster analysis and that provides the most direct information about the dynamics of the intracluster gas. X-ray analysis of intracluster gas bulk velocities became technically feasible only recently, after the calibration of the instrumental gain of the *Advanced Satellite for Cosmology and Astrophysics* (*ASCA*) spectrometers was completed. The first direct detections of intracluster gas bulk velocities were found for the Perseus and Centaurus Clusters (DB01a; DB01b) using *ASCA* data. In the case of Centaurus, a relatively high velocity gradient (~3000 km s^{-1}) was detected near the cluster's core with the Solid-State Imaging Spectrometers (SISs), which are the *ASCA* spectrometers with the best gain stability and spectral resolution.

Given the importance of velocity gradients to understanding the dynamics of the intracluster gas, it is crucial to confirm and improve the measurements of bulk velocities in these clusters. The *Chandra X-Ray Observatory* satellite provides an excellent opportunity for this task. It has good gain temporal stability (Grant 2001), and we can eliminate the spatial variations of the intrachip gain by performing spatially resolved spectroscopy of multiple cluster regions using the *the same CCD location*. In this paper, we present results of a double-pointing observation of Centaurus specifically designed for bulk gas velocity measurements.

2. PREVIOUS VELOCITY STUDIES ON CENTAURUS

Centaurus (Abell 3526) is a Bautz-Morgan type I cluster, has an optical redshift of 0.0104, and is one of the closest X-ray–bright clusters of galaxies. The temperature of the gas in the cluster is ~3.6 keV (e.g., Peres et al. 1998) and decreases toward the center to ~1 keV (Sanders & Fabian 2002). *ASCA* Gas Imaging Spectrometer (GIS) and SIS analyses of the central region of Centaurus have shown evidence of a strong central metal abundance enhancement (Fukazawa et al. 1994) varying from supersolar near the central regions down to 0.3 solar at ~13′ (1′ at the Centaurus distance is equivalent to ~19 h_{50}^{-1} kpc). At very small radii ($\lesssim 0.'5$–1′) there is significant substructure seen in surface brightness (plumes), temperature, and metal abundances (Sanders & Fabian 2002; Fabian et al. 2005). At large radii the cluster

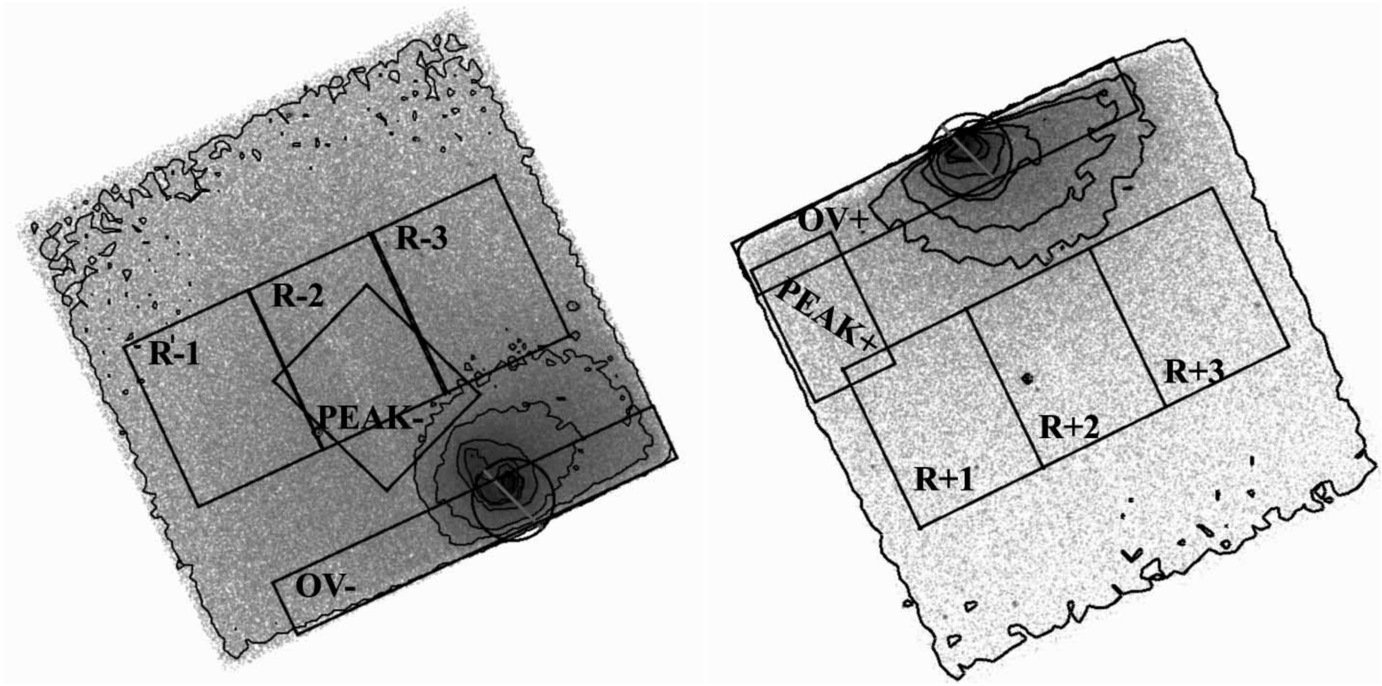

FIG. 1.—Extraction regions used for spectral fittings for the two pointings with ACIS-S3 analyzed in this work overlaid on the smoothed X-ray image. North is up for both pointings. *Left:* "Minus" pointing. The scale in right ascension is 192°.375–192°.15 (*left to right*) and in declination is −41°.36 to −41°.18 (*top to bottom*). *Right:* "Plus" pointing. The scale in right ascension is 192°.30–192°.05 (*left to right*) and in declination is −41°.28 to −41°.45 (*top to bottom*). The cluster's center is marked with a circle. X-ray contours are overlaid near the core, and we also roughly show the chip borders with a near zero surface brightness contour.

shows signs of interaction (Churazov et al. 1999) with a subgroup (Cen 45) discovered optically (Lucey et al. 1986a, 1986b; Stein et al. 1997). The main group (Cen 30), which is centered on the cD galaxy NGC 4696, shows an average radial velocity of $\sim$3400 km s^{-1} and a velocity dispersion of $\sim$900 km s^{-1}. It is accreting the Cen 45 group, which is associated with the galaxy NGC 4709 at $\gtrsim 15'$ from NGC 4696 and has an average radial velocity of $\sim$4700 km s^{-1} and a velocity dispersion of $\sim$150 km s^{-1}. The velocity difference between Cen 45 and the main body of Centaurus found in the optical frequencies ($\sim$1500 km s^{-1}) was also corroborated in X-rays (DB01b). DB01b also used the SIS on *ASCA* to study the intracluster gas properties at intermediate spatial scales ($\sim 3'$–$8'$). They found a strong velocity gradient in both SIS0 and SIS1. The maximum velocity difference was found to be $(3.3 \pm 1.1) \times 10^3$ km s^{-1} along the direction perpendicular to that of the incoming subgroup Cen 45, and they argued that it is likely due to a prior merging event with a strong line-of-sight component in the Centaurus cluster.

3. DATA REDUCTION AND ANALYSIS

Abell 3526 off-center pointings analyzed in this work were observed using *Chandra*'s Advanced CCD Imaging Spectrometer 3 (ACIS-S3) on 2003 April 18, for 35 ks each. After removal of high-background periods we were left with 34.3 and 33.9 ks for the two pointings. Both observations were performed consecutively. In both cases the CCD was centered on the regions of expected maximal departure from the systemic velocity as derived from a previous *ASCA* analysis (DB01b). The spatial configuration of the regions analyzed in this work and the relative location of the cluster's center with respect to the ACIS-S3 chip are shown in Figure 1. Here we focus on the results of the central CCD regions, which are at the same CCD coordinates but still far enough from the spectroscopically complex cluster core. The use of the same CCD coordinates to study the regions of interest allows us to improve the accuracy of the measured gas velocities, since the intrachip gain variations are minimized.

We used CIAO version 3.2.2 with CALDB version 3.0.3 to screen the data. The data were cleaned using the standard procedure.[1] Grades 0, 2, 3, 4, and 6 were used. The ACIS particle background was cleaned as prescribed for VFAINT mode. A gain map correction was applied, together with pulse height analyzer and pixel randomization. Point sources were extracted, and the background used in the spectral fits was generated from blank-sky observations using the `acis_bkgrnd_lookup` script. Here we show the results of spectral fittings with XSPEC version 11.3.1 (Arnaud 1996) using an absorbed VAPEC thermal emission model. Metal abundances are measured relative to the solar photospheric values of Anders & Grevesse (1989). Galactic photoelectric absorption ($N_{\rm H}$) was incorporated using the `wabs` model (Morrison & McCammon 1983). Spectral channels were grouped to have at least 20 counts per channel. Energy ranges were restricted to 0.5–8.5 keV. The spectral fitting parameter errors are 1 σ unless stated otherwise.

There is a known reduction of quantum efficiency due to molecular contamination buildup on the optical blocking filter (or on the CCD chips),[2] which affects the count rates significantly at energy ranges below 1 keV. This also affects determination of low-energy lines' abundances, hydrogen column density, and overall gas temperature. Previously corrected with the ACISABS model or `corrarf` routine, this correction is now done automatically within the `mkwarf` routine. The use of the newly incorporated routines significantly reduced the intrachip scatter of the recovered value of $N_{\rm H}$ across the detectors. The overall value of $N_{\rm H}$ was near (within 10%) Galactic, and we therefore fixed it

[1] See http://cxc.harvard.edu/ciao/guides/acis_data.html.
[2] See http://cxc.harvard.edu/cal/Links/Acis/acis/Cal_prods/qeDeg/index.html.

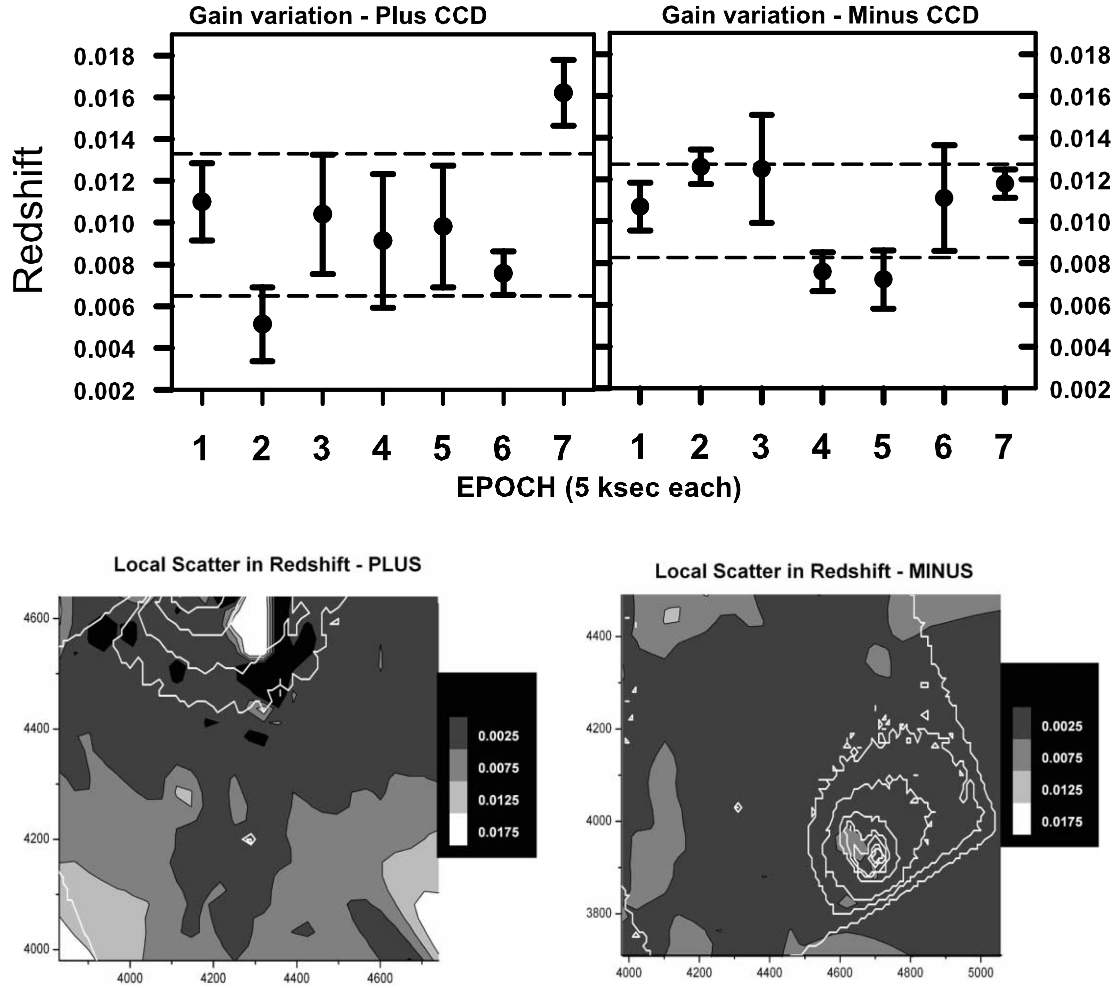

FIG. 2.—*Top:* Gain variation for the whole CCD corresponding to the two observations, "plus" (*left*) and "minus" (*right*), in seven different epochs. The dashed black horizontal lines show the standard deviation of the best-fit values. *Bottom:* Maps of the standard deviation of the best-fit velocity found in each of the seven epochs for "plus" (*left*) and "minus" (*right*). The color step represents the 1 σ fitting error for the measured redshift. The spatial scales of the two panels are different because of the intrinsically lower brightness of the "plus" side and the fact that the velocities are found using an adaptive smoothing routine that keeps the minimum number of counts fixed, therefore requiring larger region sizes for the "plus" side. The coloring outside the CCD borders is an artifact of the gridding routine and should be ignored.

at the Galactic value (8×10^{20} cm^{-2}) for all spectral fittings presented here. We hereafter refer to the observation in which *ASCA* found low velocities (northeast pointing) as "minus" (Fig. 1, *left*) and the observation in which *ASCA* found high velocities (southwest pointing) as "plus" (Fig. 1, *right*). In Figure 1 we indicate the regions used in this work for spectral extraction of each CCD on the X-ray image. We also overlay the X-ray contours showing the central regions and the CCD border.

3.1. *ACIS-S3 Temporal and Spatial Gain Stability*

In order to estimate the level of global temporal gain fluctuations in both observations for the regions of interest, we divided each event file into seven different time intervals, with about 5 ks in each interval. We used a region corresponding spatially to the full CCD with $\sim 1'$ borders excluded. We then extracted spectra and determined the best-fit parameters. We show the results in Figure 2 (*top*) for the redshifts. It can be seen that the plus pointing has been affected by stronger fluctuations than the minus pointing. The minus pointing shows a significantly smaller overall redshift scatter. The temporal variation of the gain increases the overall uncertainties of the velocity analysis differently in each pointing. We included in quadrature the standard deviation of the gain scatter over time in the final estimation of the velocity gradients.

We can also estimate the change in intrachip gain fluctuations within the observation by looking at the velocity change in different positions of the CCD. Using the same event files obtained for the seven different epochs as those described in the previous paragraph, we determined a velocity map through an adaptive smoothing routine that keeps a fixed minimum number of counts per region (here we used 5000 counts) to keep the range of fitting errors more or less constant for different regions. We then determined the standard deviation of the best-fit velocities for the same region through different time periods. We plot the results in Figure 2 (*bottom*), where regions of high scatter are brighter. The color steps in Figure 2 (*bottom*) represent the standard deviation of the best-fit redshifts of the individual regions used to construct the velocity map. Given the limited photon statistics, the precision with which we can determine the variations is relatively poor. Nevertheless, it can be seen that the plus observation is also more affected by intrachip temporal gain variations, especially near the southeast, partially including the R + 1 region. In the minus side the region most affected by the intrachip temporal gain fluctuation is R − 1. Overall, the regions chosen for velocity analysis , i.e., along the "strip" (see below), PEAK− and PEAK+, do not encompass regions of very high gain instability.

In order to check for any global gain shift between observations, we used the part of the CCDs that corresponds to the

TABLE 1
BEST-FIT REDSHIFTS FOR THE "SKY" OVERLAPPING REGIONS

Parameter	Value with Core			Value without Core		
	0.5–8.5 keV	1.0–8.5 keV	0.5–5.0 keV	0.5–8.5 keV	1.0–8.5 keV	0.5–5.0 keV
$z_{\rm OV+}$ (10^{-2})................	1.285 ± 0.015	0.91 ± 0.016	1.29 ± 0.025	0.895 ± 0.02	0.91 ± 0.04	1.175 ± 0.075
$z_{\rm OV-}$ (10^{-2})...............	2.256 ± 0.07	1.525 ± 0.015	2.20 ± 0.02	1.30 ± 0.02	1.287 ± 0.03	1.54 ± 0.015
ΔV (10^3 km s^{-1})	2.91 ± 0.22	1.92 ± 0.07	2.73 ± 0.11	1.22 ± 0.09	1.13 ± 0.15	1.1 ± 0.23
χ^2/dof+......................	463/299	240/265	405/258	236/268	195/234	205/236
χ^2/dof−	852/298	238/264	817/258	220/263	166/229	187/233

NOTE.—The fits are to a wabs VAPEC spectral model, and the errors are 1 σ confidence.

same "sky" regions. We call them "overlap regions" and denote them by OV− (in the minus pointing) and OV+ (in the plus pointing) in Figure 1. We present the results of the redshift variation for different cases (different spectral ranges, with core included/excluded) in Table 1. It can be seen in Table 1 that there are significant changes in the best-fit values for velocities in the overlapping regions of both pointings. The discrepancy between different pointings can be as high as $\sim 3 \times 10^3$ km s^{-1}. However, this extreme value only happens when the cluster core region is included and the soft energy band (<1 keV) is used in the spectral fittings. Given that the χ^2 values of these fittings are unacceptably high, it is clear that a simple VAPEC model cannot accurately describe the physics of the cluster core and that its inclusion is biasing the redshift measurements (see Dupke & Bregman 2005 for a description of redshift biases due to spectral modeling). Furthermore, directly fitting the iron lines with Gaussian functions produces results for the velocity differences that are similar to those obtained through spectral fittings when the core is excluded. For the Fe L complex (from 0.95 to 1.25 keV) a best-fit difference of $(1.12 \pm 0.8) \times 10^3$ km s^{-1} is found, while for the Fe K complex we find a value of $(1.47 \pm 0.54) \times 10^3$ km s^{-1}.

The error-weighted average (spectral fits without the core, Fe L, and Fe K complex) for the gain correction between observations is $(1.23 \pm 0.09) \times 10^3$ km s^{-1}. This global gain shift is most likely due to residual errors in the default correction for a nonuniform quantum efficiency degradation that are still present in the new calibration and also because the overlapping regions do not overlap in "CCD" coordinates and are at opposite locations with respect to the frame store. If we applied this global gain shift to the whole CCD the result would be a "boost" of the velocity gradient by $\sim 1.2 \times 10^3$ km s^{-1}. However, given the uncertainties for intrachip gain fluctuations we conservatively do not use this correction to boost the redshifts of the plus region, but we point out that the velocity gradient that we obtain can be seen as a lower limit.

4. VELOCITY DISTRIBUTION ALONG THE CCD TARGETED REGIONS

The main advantage of the observational strategy used here is that we can use the same regions in CCD coordinates to analyze the "sky" regions previously suspected of having discrepant velocities. By using the same CCD region we can, in principle, eliminate spatial gain variations. Temporal variations of gain are also minimized by performing the two observations consecutively. The residual gain variations between the two observations can also be estimated using the overlapping regions as shown in the previous section. The final velocity measurements should only be affected by short-term random local (subregions inside the CCD) gain variations.

We chose a strip of similar rows near the CCD center to perform a detailed spectroscopic analysis of gas velocities. This choice was based on the degradation of quantum efficiency with chip row[3] and also on the intrinsic spectral differences of the ICM between regions near the cluster's core and regions >2′ from the center. The "strip" is the most reliable region because it avoids the cluster's core and also regions at very different distances from the frame store. It also covers the most stable region for intrachip gain (Fig. 2, *bottom*). Due to the surface brightness asymmetric distribution and the higher uncertainties involved in the plus dimmer pointing we chose the size of the regions to encompass at least 15 kcounts each. In the minus observation we show the results for spectral fittings using similar sizes, and in general they have twice as many counts as their counterparts on the plus side (22, 30, and 30 kcounts for R − 1, R − 2, and R − 3, respectively). The same analysis using thinner (by a factor of 2) region sizes for the minus observation does not change the results presented here. We also avoid including the CCD borders, maintaining a margin of $\sim 30''$ from them.

The results of the spectral fittings for the strip are shown in Table 2. Without any corrections for the overall gain difference between the pointings, the regions with maximum velocity difference are R − 2 with a best-fit redshift of 0.0084 and R + 3 with $z \sim 0.0163$ corresponding to a velocity difference of $\sim (2.4 \pm 1.0) \times 10^3$ km s^{-1}, consistent with the maximum velocity differences found by *ASCA*. These two regions have similar temperatures (~3.6 keV), and the iron abundance of the high-velocity region is slightly lower (0.7 solar) than that of the low-velocity region (1 solar).

[3] See http://cxc.harvard.edu/cal/Acis/Cal_prods/qeu/qeu.pdf.

TABLE 2
SPECTRAL LINE FITTINGS FOR CENTRAL CCD REGIONS OF THE PLUS AND MINUS POINTINGS

Region	Temperature (keV)	Fe Abundance[a] (solar)	Redshift (10^{-2})	χ^2/dof
R − 1	$3.74^{+0.11}_{-0.14}$	$1.00^{+0.13}_{-0.05}$	$1.27^{+0.05}_{-0.09}$	266/293
R − 2	3.58 ± 0.11	$0.98^{+0.11}_{-0.07}$	$0.84^{+0.25}_{-0.14}$	255/317
R − 3	$3.34^{+0.10}_{-0.08}$	$0.95^{+0.10}_{-0.06}$	1.23 ± 0.08	296/317
R + 1	3.79 ± 0.20	$0.55^{+0.12}_{-0.08}$	$0.92^{+0.71}_{-0.19}$	203/253
R + 2	$3.71^{+0.16}_{-0.18}$	$0.85^{+0.13}_{-0.09}$	$0.73^{+0.15}_{-0.50}$	196/269
R + 3	$3.61^{+0.20}_{-0.22}$	$0.67^{+0.17}_{-0.09}$	$1.63^{+0.20}_{-0.34}$	193/259
PEAK−	$3.43^{+0.09}_{-0.05}$	$1.03^{+0.05}_{-0.08}$	$0.61^{+0.05}_{-0.06}$	233/295
PEAK+..........	$3.80^{+0.21}_{-0.22}$	$0.71^{+0.15}_{-0.14}$	$1.58^{+0.18}_{-0.30}$	118/198

NOTE.—The results are shown for the full energy range (0.5–8.5 keV), and the errors are 1 σ confidence.
[a] Photospheric value (Anders & Grevesse 1989).

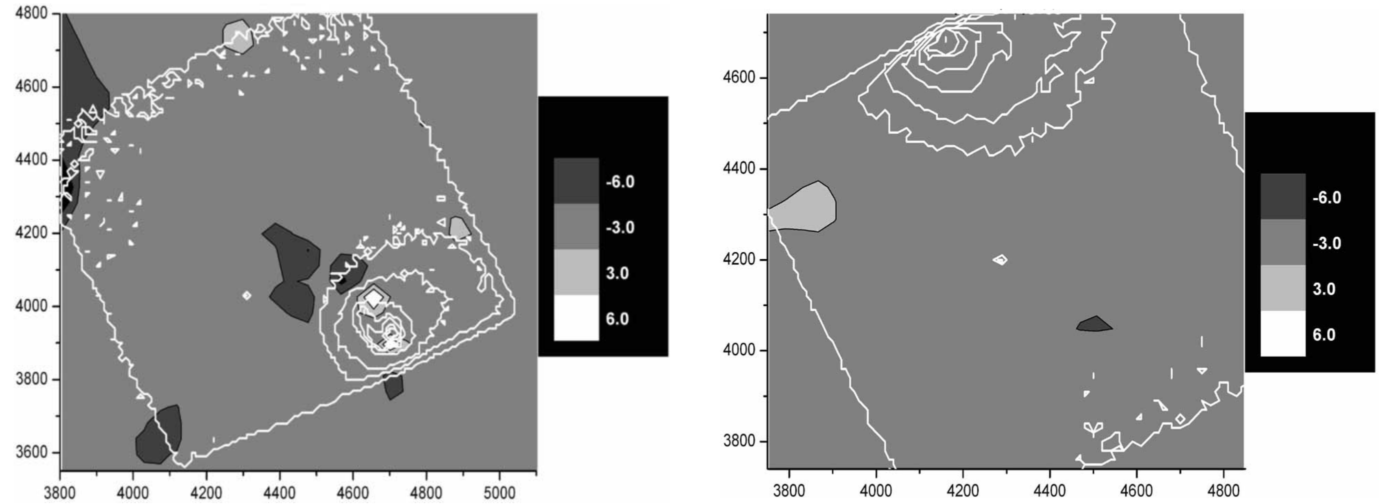

Fig. 3.—Deviation significance derived from an adaptive smoothing algorithm with a minimum of 5000 counts per extraction circular region and fitted with an absorbed VAPEC spectral model showing the significance $(z - \langle z \rangle)/\delta z$. The gridding method used is a correlation method that calculates a new value for each cell in the regular matrix from the values of the points in the adjoining cells that are included within the search radius. With the minimum count constraints the matrix size was 30×30 cells. We also overlay the X-ray contours shown in Fig. 1 on top of the color contour plot. See text for details.

Although the velocity determination is highly driven by the Fe K line at ~6.7 keV, we can also determine velocities without the Fe K line complex. Since the gain corrections are frequency dependent, the best-fit redshift determined from low-energy spectral lines can be significantly different from that determined at high frequencies. However, the differences for both regions were changed similarly so that the velocity *differences* were maintained. For example, the regions R − 2 and R + 3 had their best-fit redshifts changed to $(1.08 \pm 0.23) \times 10^{-2}$ and $(1.83 \pm 0.30) \times 10^{-2}$, respectively, when the Fe K region was excluded from the spectral fittings. The resulting velocity difference $(2.25 \pm 1.13) \times 10^3$ km s^{-1} is virtually identical to that derived with the inclusion of the Fe K line complex.

5. REGIONS OF MAXIMUM VELOCITY GRADIENT

Despite the apparent overall gain shift between the observations and the difference in photon statistics, we can estimate the velocity signals with the highest statistical significance by dividing the difference of the best-fit velocity from the average over the CCD by the error of the measured velocity. We call this error-weighted deviation simply "deviation significance" and plot its color contours in Figure 3. In Figure 3 the black and white represent negative and positive velocities, respectively, with respect to the CCD average velocity. The magnitude of the deviation significance shows how significant is the velocity structure. This allows us to probe the significance "peaks" for further analysis.

From Figure 3 (*left*) we can see that in the minus pointing there is a significant low-redshift (blueshifted) zone that extends from the outer contours of the cluster's core (>1.′5) toward the middle of the CCD (~3′–4′ from the cluster core) significantly overlapping with the R − 2 region and also with the low-redshift zone P3 found with *ASCA* by DB01b. In Figure 3 (*left*) we also see two relatively small redshifted regions on each side of the core of the cluster but at very small distances: one at the tip of the nuclear X-ray arm (<1′ from the core) and the other at <30″ south of the core. As mentioned above, the proximity to the cluster core reduces the reliability of the best-fit velocities found with the methodology used here. Furthermore, the projected temperature in that region is very low (1.0–1.4 keV), and the Fe K line complex is unseen. On the other hand, the redshift of the more extended blueshifted region near the CCD center is determined mostly from the Fe K line given the higher temperatures (3–3.8 keV). Since the spatial gain variations are in general frequency dependent, we should not directly compare redshifts determined from Fe L with those from Fe K lines, and conservatively we do not consider the velocity results from spectral fittings of regions that are too close (<1′) to the cluster's center. The plus pointing (Fig. 3, *right*) is in general more featureless but shows a relatively extended region of high velocities toward the southeast of the cluster relatively near the detector's edge. The significance of this positive-velocity region is smaller than that of the blueshifted region in the minus pointing.

The upper limit for the velocity gradient in the Centaurus cluster can be estimated from a more detailed analysis of the regions surrounding the high significance peaks of Figure 3. We selected for that purpose two regions shown in Figure 1 as PEAK+ and PEAK−. They are both rectangular regions 2.′3 × 2.′7 (PEAK−) and 1.′5 × 2.′5 (PEAK+) located 2.′7 (PEAK−) and 3.′7 (PEAK+) away from the cluster's center, respectively, out of the core region. Individual spectral fittings of these two regions show mildly different temperatures and Fe abundance (Table 2). PEAK− has a temperature of 3.43 keV and a solar Fe abundance, while PEAK+ is slightly hotter with a temperature of 3.80 keV and an abundance of 0.7 solar. The redshifts of these two regions are significantly discrepant, as expected, and correspond to a velocity difference of $(2.9 \pm 0.7) \times 10^3$ km s^{-1}. The 90% and 99% confidence contours for these two regions are shown in Figure 4 (*left*), together with the line of equal redshifts. The *F*-test indicates that the redshifts are different at 99.4% confidence, where the χ^2 of simultaneous spectral fittings of both regions with tied redshifts declines from 355.3 to 349.9 for 494 degrees of freedom when the redshifts of the two data groups are let free to vary.

It should be noted that although these regions show the most significant velocity gradient observed in the two pointings, PEAK+ does not overlap with the strip analyzed in § 4 that included regions R + 1, R + 2, and R + 3. The region in that strip that is the closest to PEAK+ is R + 1. The large positive error bar of the best-fit redshift measured for that region is due to a second minimum in χ^2 space near the same redshift value as PEAK+, which suggests that this high-velocity region may extend to and partially overlap with

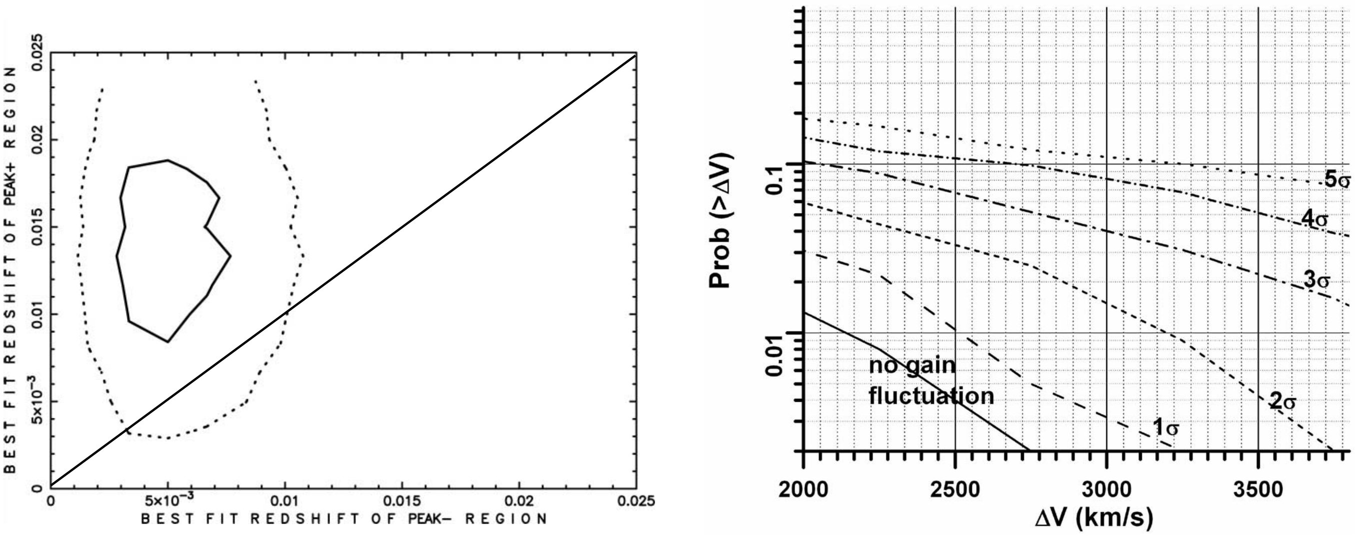

FIG. 4.—*Left:* Confidence contour plot for the redshifts measured for the PEAK+ and PEAK− extraction regions. The two contours correspond the 90% (*dashed line*) and 99% (*dotted line*) confidence levels. The contours are found from simultaneous spectral fittings of two data groups corresponding to the PEAK+ and PEAK− regions. We also indicate the line of equal redshifts. *Right:* Probability of detecting a velocity difference greater than ΔV for the PEAK+ and PEAK− regions. The solid line indicates no gain fluctuations. The other plots assume a 1 σ (*dashed line*), 2 σ (*short-dashed line*), 3 σ (*long-dash–dotted line*), 4 σ (*short-dash–dotted line*), and 5 σ (*dotted line*) gain fluctuation (1 σ corresponds to 500 km s^{-1} for individual velocity differences). Results are obtained from spectral fittings of 1000 simulated spectra for each region.

R + 1. Unfortunately, local temporal gain fluctuations are relatively high in R + 1 (Fig. 2, *bottom left*), and with the available observations, there are not enough photon statistics to disentangle multiple velocity components in the line of sight spectroscopically.

To determine the level of gain fluctuations necessary to blur the detected velocity difference found between PEAK− and PEAK+, we used the Monte Carlo method. We performed 1000 simulations corresponding to PEAK− and PEAK+ using the XSPEC tool `fakeit`. We input the same initial parameter values as those found for the real data except for the redshifts, which were initially set at some intermediate value (0.011). Background and responses corresponding to the real observations were also included, and Poisson errors were added. The results are shown in Figure 4 (*right*), where we plot the probability that the velocity difference between PEAK+ and PEAK− is greater to or equal than the value shown in the *x*-axis. It can be seen that for the velocity gradient to be generated by chance (assumed here as <84%) it would be necessary to have a $\gtrsim 5\ \sigma$ gain fluctuation corresponding to an uncertainty of $\gtrsim 2500$ km s^{-1} in the velocity difference (or $\gtrsim 0.6$% gain uncertainty per velocity measurement), which is significantly higher than that seen across the CCDs.

6. SUMMARY AND DISCUSSION

In this work we report the analysis of velocity structures in the intracluster gas of the Centaurus cluster at spatial scales smaller than (but comparable to) that used in a previous *ASCA* analysis. The two off-center pointings were taken in such a way as to minimize the temporal intrachip gain variations, which is crucial when performing velocity tomography of the ICM with X-ray CCDs. Our analysis of the gain stability suggests that the intrachip gain variability is higher than that measured before 2001 (Grant 2001), limiting the precision of the measured velocity differences. We have confirmed the detection of a significant velocity gradient in the Centaurus cluster along a direction roughly perpendicular to the direction toward the Cen 45 subgroup. There is some uncertainty on the uniqueness of the direction of the velocity gradient, and there are indications that the high-velocity region may extend to the south. The gradient is also seen in individual spectral lines belonging to Fe L and Fe K line groups but with higher uncertainties.

Velocity gradients, both transitory and rotational, can be caused by cluster mergers (e.g., Roettiger et al. 1997; Ricker 1998; Takizawa & Mineshige 1998). If the gradient is due to residual gas circulation around the cluster's center, the corresponding circular velocity ($V_{\rm circ}$) is $(1.2 \pm 0.7) \times 10^3$ km s^{-1} as derived from spectral fittings of the full spectra of regions R − 2 and R + 3, where we include the local temporal gain variation in the errors. This is consistent with subsonic (transonic) gas motion given by $(5kT_{\rm ICM}/3\mu m_p)^{1/2} \approx 10^3 (T_{\rm keV}/3.7\ {\rm keV})^{1/2}$ km s^{-1}. This kind of configuration for the velocity gradient is further supported by the lack of other indications of supersonic gas motions in the region analyzed, such as bow shocks. Such circulation, either rotational or eddylike (such as that predicted by Ricker & Sarazin 2001), is suggestive of past off-center mergers with a strong component near the line of sight toward Centaurus (Churazov et al. 1999; DB01b). The velocity difference in the zones of maximum significance can be as high as $(2.9 \pm 0.7) \times 10^3$ km s^{-1}. However, these zones are discrepant in CCD coordinates, and spatial-temporal gain variations cannot be ruled out as a factor for amplifying the velocity gradient. If the intrachip gain uncertainties (from Fig. 2, *bottom left*) are incorporated in the velocity measurements in the regions of maximum significance, the errors in velocity difference would nearly double ($\sim 2.5 \times 10^3$ km s^{-1}).

From the measurements shown here we can estimate the relative importance of the velocity gradient as measured from R − 2 and R + 3. Assuming that the gas is uniformly rotating around the cluster's center at a distance R, the circulation time is $\tau \sim (0.44\ h_{50}^{-1})(R/4\farcm5)(V_{\rm circ}/1.2 \times 10^3\ {\rm km\ s^{-1}})^{-1}$ Gyr. In our particular case, for a cylinder at a radial distance R and with height $\approx \Delta R \approx R$, the rotational energy can be roughly given by $E_{\rm rot} \sim (2 \times 10^{61}\ h_{50}^{-3})(\eta/2.5)(\mu/0.6)(n/10^{-2}\ {\rm cm^{-3}})(V_{\rm circ}/1.2 \times 10^3\ {\rm km\ s^{-1}})^2 (R/4\farcm5)^3$ ergs, where n is the gas particle number density, μ is the mean molecular weight, and η is a geometric coefficient such that $\eta = I/MR^2$, where I is the moment of inertia and M the mass of the rotating body. Since the typical energy of cluster mergers is 10^{63}–10^{64} ergs and considering that we are probing only a small region of the cluster, our results imply that >0.1%–1% of the total merging mechanical energy can still be effectively converted into kinetic $\gtrsim$0.3–0.6 Gyr after the merging event. The ratio of bulk kinetic to thermal gas energies is given by $\beta_{\rm gas} = 2(\eta/2.5)(\mu/0.6)(V_{\rm circ}/1.2 \times 10^3\ {\rm km\ s^{-1}})^2 \times (kT/3.7\ {\rm keV})^{-1} \gtrsim 1$, implying that the X-ray–derived mass within the region analyzed can be significantly underestimated if this high level of departure from hydrostatic equilibrium is not taken into account. This work suggests that the intracluster gas can significantly depart from hydrostatic equilibrium even in cool clusters that do not show strong signs of merging, such as Abell 3526.

The consistency between *Chandra* and *ASCA* measurements of the velocity field illustrates the ability of current spectrometers to measure intracluster gas bulk motions with relatively short observations. Furthermore, with the demise of the calorimeter on board *Suzaku*, it is clear that the study of ICM velocity gradients depends heavily on multipointing observations made with different X-ray spectrometers, allowing us to reduce gain systematics and cross-check the measurements.

We would like to thank E. Lloyd-Davies and J. Irwin for the many helpful discussions and suggestions. We particularly thank Catherine Grant, George Chartas, and Alexey Vikhlinin for providing helpful information on calibration issues. We acknowledge support from NASA grants NAG5-3247 and AR4-5013X. This research made use of the HEASARC *ASCA* database and NED.

REFERENCES

Anders, E., & Grevesse, N. 1989, Geochim. Cosmochim. Acta, 53, 197
Arnaud, K. A. 1996, in ASP Conf. Ser. 101, Astronomical Data Analysis Software and Systems V, ed. G. Jacoby & J. Barnes (San Francisco: ASP), 17
Burns, J. O., Loken, C., Roettiger, K., Rizza, E., Bryan, G., Norman, M. L., Gómez, P., & Owen, F. N. 2002, NewA Rev., 46, 135
Churazov, E., Gilfanov, M., Forman, W., & Jones, C. 1999, ApJ, 520, 105
Dupke, R. A., & Bregman, J. N. 2001a, ApJ, 547, 705 (DB01a)
———. 2001b, ApJ, 562, 266 (DB01b)
———. 2002, ApJ, 575, 634
———. 2005, ApJS, 161, 224
Evrard, A. E. 1990, ApJ, 363, 349
Evrard, A. E., Metzler, C. A., & Navarro, J. F. 1996, ApJ, 469, 494
Fabian, A., Sanders, J. S., Taylor, G. B., & Allen, S. W. 2005, MNRAS, 360, L20
Fujita, Y., Matsumoto, T., & Wada, K. 2004, ApJ, 612, L9
Fukazawa, Y., Ohashi, T., Fabian, A. C., Canizares, C. R., Ikebe, Y., Makishima, K., Mushotzky, R. F., & Yamashita, K. 1994, PASJ, 46, L55
Grant, C. 2001, ACIS Memo 195 (Cambridge: MIT), http://space.mit.edu/ACIS/ps_files/ps195.ps.gz
Katz, N., & White, S. D. M. 1993, ApJ, 412, 455
Lucey, J. R., Currie, M. J., & Dickens, R. J. 1986a, MNRAS, 221, 453
Lucey, J. R., Currie, M. J., & Dickens, R. J. 1986b, MNRAS, 222, 427
Morrison, R., & McCammon, D. 1983, ApJ, 270, 119
Navarro, J. F., Frenk, C. S., & White, S. D. M. 1995, MNRAS, 275, 720
Pawl, A., Evrard, A., & Dupke, R. A. 2005, ApJ, 631, 773
Pearce, F. R., Thomas, P. A., & Couchman, H. M. P. 1994, MNRAS, 268, 953
Peres, C. B., Fabian, A. C., Edge, S. W., Johnstone, R. M., & White, D. A. 1998, MNRAS, 298, 416
Ricker, P. M. 1998, ApJ, 496, 670
Ricker, P. M., & Sarazin, C. 2001, ApJ, 561, 621
Roettiger, K., Burns, J. O., & Loken, C. 1993, ApJ, 407, L53
———. 1996, ApJ, 473, 651
Roettiger, K., & Flores, H. 2000, ApJ, 538, 92
Roettiger, K., Loken, C., & Burns, J. O. 1997, ApJS, 109, 307
Roettiger, K., Stone, J. M., & Mushotzky, R. 1998, ApJ, 493, 62
Sanders, J. S., & Fabian, A. 2002, MNRAS, 331, 273
Stein, P., Jerjen, H., & Federspiel, M. 1997, A&A, 327, 952
Sunyaev, R. A., Norman, M. L., & Bryan, G. L. 2003, Astron. Lett., 29, 783
Takizawa, M. 1999, ApJ, 520, 514
———. 2000, ApJ, 532, 183
Takizawa, M., & Mineshige, S. 1998, ApJ, 499, 82